Experimental investigation of heat transfer in a subscale liquid rocket engine at high mixture ratio.

Philippe Grenard, Nicolas Fdida, Lucien Vingert, Luc-Henry Dorey, Laurent Selle, Julien Pichillou

Experimental investigation of heat transfer in a subscale liquid rocket engine at high mixture ratio.

P. Grenard * and N. Fdida † and L. Vingert ‡ and L.H. Dorey §
ONERA - The French Aerospace Lab, 91761 PALAISEAU, FRANCE

L. Selle ¶
CNRS, 31400 Toulouse, FRANCE

J. Pichillou ‖
CNES, 52 rue Jacques Hillairet, 75012 Paris Cedex, FRANCE

This work presents the experimental investigation of heat fluxes through the walls of a reduced-scale rocket motor using hydrogen and oxygen as propellants. The engine is water-cooled so that it can be run in steady state for up to 120 s. More than 100 thermocouples are used to retrieve wall temperature and derive heat fluxes. It is shown how the chamber pressure affects the overall heat-flux level, while the mixture ratio greatly influences its distribution. Direct visualisation of the flame provides an indication that the heat-flux distribution is correlated to the location of heat release given by OH* visualization.

I. Introduction

In rocket engines using cryogenic reactants, the combustion of the fuel in pure oxygen yields very high temperatures in the combustion chamber. Indeed, the combination of extreme thermodynamic conditions and diffusion flames burning around stoichiometry may produce pockets of burnt gases above 3500 K [1]. If such hot pockets reach the combustion chamber walls, it results in extreme heat fluxes and potentially high temperatures that may exceed the thermal resistance of the material. For engines that need to operate for long times or are required to withstand multiple restarts, the accurate prediction of chamber wall temperature is of paramount importance. Quoting Fröhlich et al. [2], ' [...] a mistake of 40K [leads] to a 50% reduction of life' for cycle life and creep apparition predictions. Similarly, in the framework of reusable engines, the lifetime of the combustion chamber and its maintenance costs are directly linked to the precise knowledge of wall temperature. Also, in the case of regeneratively cooled rocket engines, the fuel is used to cool the combustion chamber prior to its injection and combustion. The performance of the engine is then directly linked to the heat exchange within the cooling channels. Obviously, the robustness and reliability of the engine

*Research Engineer, Multiphysics for Energetics Department, philippe.grenard@onera.fr
†Ph.D., Research Engineer, Multiphysics for Energetics Department
‡Research Engineer, Multiphysics for Energetics Department
§Ph.D., Research Engineer, Multiphysics for Energetics Department
¶Ph.D., CNRS Research fellow, IMFT
‖Aerospace Engineer, DLA

is something that can not be compromised, but on the other hand, excessive design margins are likely to increase its size and weight, resulting in an overall reduction of the launcher's efficiency. Consequently, the modelling of heat transfer in cryogenic rocket engines is critical for a proper design with optimised performance and reliable operation.

Several research groups over the world have tackled this topic using small-scale experiments. Marshall et al studied single-injector configuration [3] while De Ridder et al focused on multi-injector configurations [4]. They have shown how the global flux scales with pressure but also that its longitudinal distribution depends on the injector arrangement and the ratio of oxidizer to fuel. Similar studies have been conducted by Conley et al [5]. By varying independently the chamber pressure and fuel mass flow rate, they questioned the direct pressure dependance and proposed a square root of the fuel mass flux law instead. The influence of the geometry (chamber length) was also highlighted. Cai et al. studied experimentally and numerically the influence of the injector design on the heat fluxes [6] while Silvestri et al. measured the influence of coaxial injector recess length on heat transfer [7]. Celano et al. also experimented single and multi-injector configurations using methane as the fuel [8]. However, most of these configurations use capacitive combustion chambers, i.e. uncooled chamber walls whose temperature increases over the duration of the hot-fire test. Cooled configurations able to reach a steady state are more rare. They are mainly based on calorimeter cooled segments where heat fluxes are deduced from enthalpy difference measurements of cooling channels. Such a setup was operated with methane and used for direct comparison with numerical simulations [9] and with both methane and hydrogen with specific focus on film cooling [10–13]. Ahn et al also used a calorimeter cooled combustion chamber to study the influence of bi-swirl injector recess length on the heat transfer at the wall for a multi-injector oxygen-kerosene configuration [14]. They propose a correlation of the heat transfer with main characteristics being combustion chamber pressure, oxygen to fuel ratio and recess length.

With the intent to improve the fundamental knowledge of heat transfer in rocket engines, as well as to provide a validation database for model and numerical simulations, Cnes and Onera have built a high-pressure, high-mixture-ratio combustion chamber, which is water cooled [15, 16]. This small-scale experiment contains five coaxial injectors arranged in a cross pattern and the operating conditions are representative of a real engine. It is operated at the Onera Mascotte test bench [17] and can reach chamber pressures up to 7 MPa under stoichiometric conditions. The injection head and combustion chamber are instrumented with over 100 thermocouples for the determination of wall temperatures and heat fluxes. The objective of this study is to characterise the influence of chamber pressure and mixture ratio r (defined as the ratio of the oxidizer and fuel mass-flow rates: $r = \dot{m}_o/\dot{m}_f$), on the heat flux distribution in the engine. A module with optical access can also be fitted on this chamber in order to visualise the influence of these conditions on the flame shape.

This paper is organised as follows: first the experimental setup is presented in Section II. The water-cooled and visualisation modules are described, as well as a typical hot-fire sequence. Then in Section III, the operating conditions and validation procedure are detailed. Finally Section IV presents the results and their discussion. Temperature and

heat-flux profiles are shown and interpreted in conjunction with direct flame visualisation.

II. Presentation of the experiment

The specifications of the present high-pressure, high-mixture-ratio combustion chamber (referred to as Bhp-HrM) are such that it can withstand long hot-fire tests with a high mixture ratio. While previous designs operated at ONERA [18] did not allow $r \geq 3$, the Bhp-HrM chamber was successfully tested for $1.9 \leq r \leq 7.7$. Also, thanks to an extensive water-cooling system, it has already been fired for as long as 120 s in steady state, at $r = 7.7$ and a chamber pressure, $P_{ch} = 6.3$ MPa.

Several versions of the chamber have been developed and two are presented here: first the so-called 'thermal version', dedicated to the measurement of heat transfer (*cf.* Sec. A), and then the 'visualization version' with optical access to the flame (*cf.* Sec. B).

A. Setup for heat transfer

A longitudinal cut through the whole engine is presented in Fig. 1(a). It consists of three main elements:

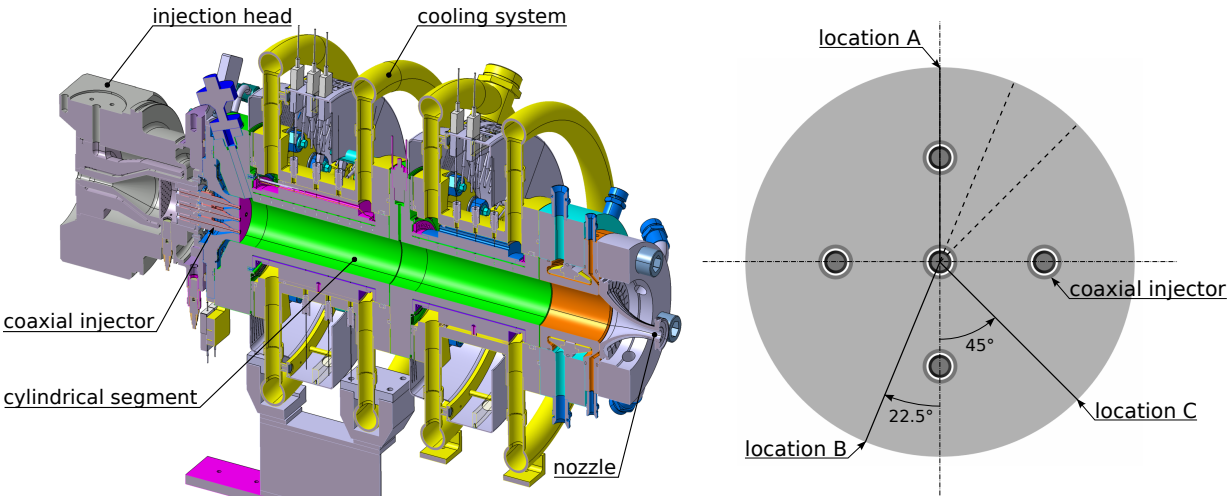

(a) Longitudinal cross-section of the whole setup.

(b) View of the injector head.

Fig. 1 Schematic of the thermal version of the experiment operated at ONERA on the Mascotte test bench.

Injection head: five shear coaxial injectors are fed with hydrogen and oxygen by two separate cavities referred to as domes. Oxygen is injected in the central tube with a diameter, d, surrounded by an annular hydrogen jet. The injectors are arranged in a cross pattern (*cf.* Fig. 1(b)) with one on the axis of the chamber and the four others, equally spaced on a 30 mm diameter circle around the central injector. Gaseous hydrogen is injected at a temperature, $T^{in}_{H_2} \sim 285$ K while oxygen is fed into the injector at $T^{in}_{O_2} \sim 300$ K. This part of the engine is either cooled (for long hot fire tests) or not cooled and instrumented with 14 thermocouples.

Combustion chamber: it consists of three water-cooled cylindrical segments of inner diameter $D_c = 56$ mm, made

of a chromium-zirconium copper-alloy. The first two segments are designed for heat transfer measurement, they have a length $L_s = 200$ mm and are fitted with thermocouples. Three azimutal locations are chosen for temperature measurements: location A is aligned with an injector, location C lies between two injectors and location B is intermediate between A and C (*cf.* Fig. 1(b)). For each of these azimutal coordinates, 17 pairs of thermocouples were brazed directely inside small drills in the walls of the combustion chamber, one of each pair on the side of the burnt gases (so-called *hot side*) and the other one on the cooling-water side (so-called *cold side*). Consequently, there is a total of 102 thermocouples, allowing the evaluation of the heat fluxes at 51 locations.

The third segment is not instrumented and has a length $L_3 = 80$ mm. The total length of the chamber is then $L_c = 2 \times L_s + L_3 = 480$ mm.

Nozzle: the engine is closed by a choked nozzle that is cooled by an internal helium film, flowing along the inner wall. In case of intense heat transfer, the nozzle can also be water-cooled by an array of longitudinal ducts on its outer side. A photograph of the experiment is presented in Fig. 2(a), on which the feeding lines of fuel, oxidizer and coolant are clearly visible, together with the wiring for the thermocouples. This setup can be operated with hydrogen or methane

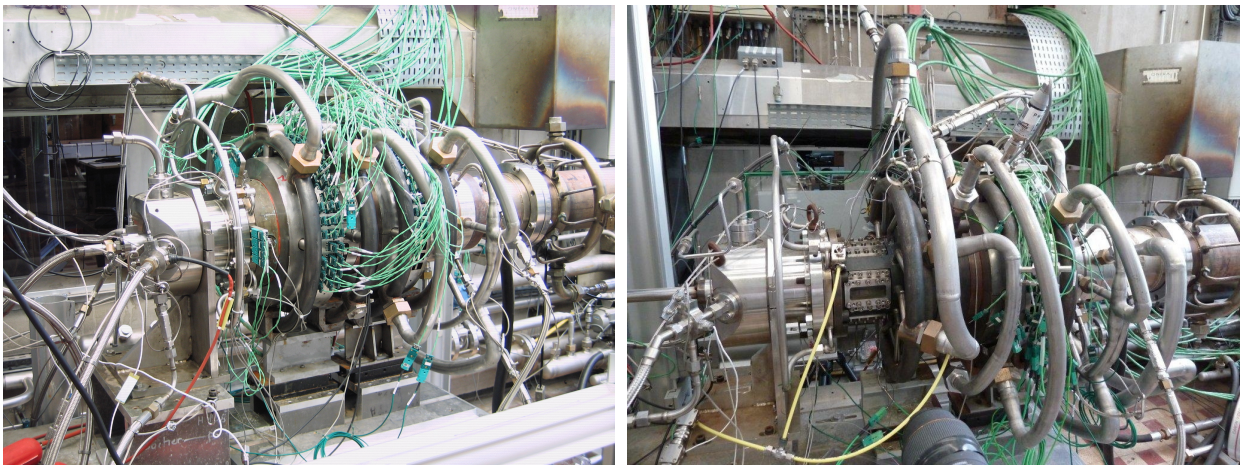

(a) Thermal version. (b) Visualization version.

Fig. 2 Photograph of the Bhp-HrM experiment operated at ONERA on the Mascotte test bench.

(gaseous or liquid) as the fuel and gaseous or liquid oxygen. The maximum combustion chamber pressure is 7 MPa, and the mixture ratio, r, of oxidiser versus fuel mass-flow rates, can be varied between 0.9 and 8 for hydrogen / oxygen combustion.

Because the scientific goal is the study of heat transfer, the design phase was particularly crucial for the choice of the materials and the sizes of each elements. Unlike classical laboratory-scale combustion experiments that can be designed with fairly large mechanical and thermal margins, this setup requires a more delicate tuning. For example, thermal equilibrium of the measurement sections must be reached over the duration of a single run for a proper evaluation of the heat fluxes by the temperature difference between the cold and hot sides.

Additionally, the extreme thermodynamic conditions typical of rocket engines raise additional technical challenges. Because of the high pressure and temperature gradients, large mechanical constraints can lead to cooling failure, excessive stress or deformation of the injectors, *etc.* All thermocouples were calibrated prior to their installation, however, the brazing procedure into the internal side of the combustion chamber is a difficult task with uncertainties on the radial location of the probe (its depth into the chamber wall). The brazing procedure may also damage the thermocouples. For these reasons, the uncertainties associated with such an experiment are expected to be larger than for atmospheric-pressure rigs. Careful validation and calibration procedures were therefore conducted, as explained in Sec. III.

B. Setup for flame visualization

The first section of the combustion chamber can be replaced by a visualization module fitted with quartz windows on all 4 sides, covering a little more than half of the module length, which are cooled by an additional helium film. This helium film is injected through a row of small tubes along the window surface and is considered to have negligible impact on the flame development inside the combustion chamber. This module is reversible : with windows placed at the upstream position, (*cf.* Fig. 2(b)), the flame is seen from its anchoring point. A flip of the visualization module puts the optical access in the downstream position, allowing the visualization of the flame tip. There is an overlap with the first region so that the whole mean flame shape can be reconstructed after two hot-fire tests.

A high-speed intensified camera was used to detect spontaneous OH* emission. The OH* radical is an intermediate species of oxygen/hydrogen combustion which is produced in the reaction (flame) zone [19]. OH* emission can be used as a direct marker of the heat release location but the emission intensity cannot be quantitatively related to the heat release without an appropriate model of OH* production [20]. OH* emission comes from two dominating physical mechanisms: the chemical excitation which is a marker of the chemical reaction of OH* in an excited state and thermal collisions of OH in its ground state with other molecules. According to [21], the OH* chemical production is dominating until the temperature reaches 2700 K and becomes negligible above 3000 K compared to OH thermal emission. In the reaction zone of such a cryogenic flame, temperatures can exceed 3000 K ([22]), so that we can consider that the dominating process producing OH* radiation is probably thermal collisions. Radiation from OH* takes place in the near UV range between 306 nm and 320 nm, according to Dieke and Crosswhite [23]. OH* emission is collected with a Photron FASTCAM Ultima APX I2 placed in front of the visualization section of the combustion chamber shown in Fig. 2(b). This system was equipped with a 10-bit CMOS sensor and an appropriate UV image intensifier for OH*. The objective was a CERCO 2085 UV of 94 mm focal length and the aperture was set to its maximum at f/4.1. An OH filter was mounted on the lens, its transmission specifications are 15% of maximum transmission at 310 nm, with 12 nm width at half height. The field of view covered the whole visualization window (66 mm $\times$ 21 mm), with a resolution of about 12.5 pix/mm, for the full frame (1024 x 512 pixels). The gain of the

intensifier was kept constant at 3 V and the exposure time of the image intensifier was adjusted (from 1.5 to 8 µs) to obtain a high signal-to-noise ratio on images. As the gain of the intensifier did not vary between operating conditions, it was assumed that the chemiluminescence signal depends linearly on the exposure time. Thus mean images were normalised by the exposure time, in order to allow a direct comparison between operating conditions. The camera frame rate was kept constant at 1,000 Hz as well as the CMOS sensor exposure time (1 ms).

A typical OH* instantaneous snapshot, recorded at 1 kHz with an exposure time of the intensifier of 3.5 ţs, is shown in Fig. 3, with the visualization module replacing the first segment. The flow is highly turbulent and the flames are strongly wrinkled. Because of the line-of-sight integration, this visualization actually encompasses the three flames

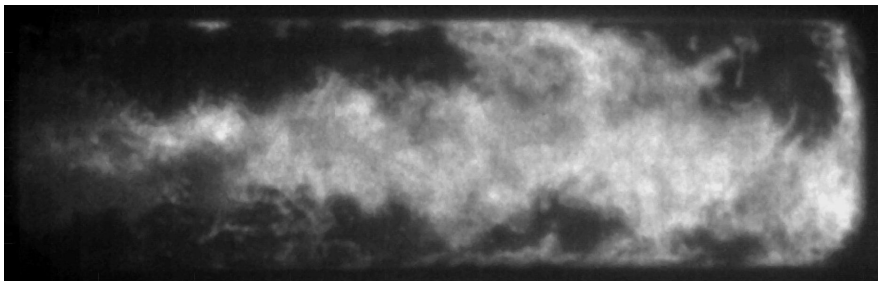

Fig. 3 Typical raw instantaneous OH* image. Case P4r2 in Tab. 1.

from the horizontal injectors. Portions of the top and bottom flames are also visible. Time average and fluctuation fields of OH* are obtained with 2, 000 snapshots recorded at a frequency of 1, 000 Hz during 2 s.

C. Hot-fire test sequence

A test sequence is initiated with the flow of helium inside the chamber and water cooling inside the segments of the combustion chamber. Then at $t = 23.5$ s, the ignition torch is activated. Figure 4 presents the evolution of reactants' mass-flow rates and chamber pressure during a typical run of the experiment. At $t = 25$ s the flows of hydrogen and oxygen are started at relatively low values, resulting in rapid ignition and a modest increase of the chamber pressure. The nominal operating point is triggered at $t = 30$ s resulting in a rapid increase of the pressure. At $t = 35$ s the closing signal is sent to the hydrogen and oxygen valves but the flow of helium is kept in order to flush the chamber. In this specific example, the chamber pressure remains steady for about 3 s during which the wall temperatures are recorded. The high-speed camera is started at $t = 23.5$ s for 12 s so that it covers the whole of ignition and steady-state operation.

III. Operating conditions and calibration

A. Operating conditions

The operating pressure, P_{ch}, in the combustion chamber can be predicted from the mass-flow rates, using the following assumptions: (1) combustion is complete, (2) the outlet nozzle is choked and (3) the heat losses through the

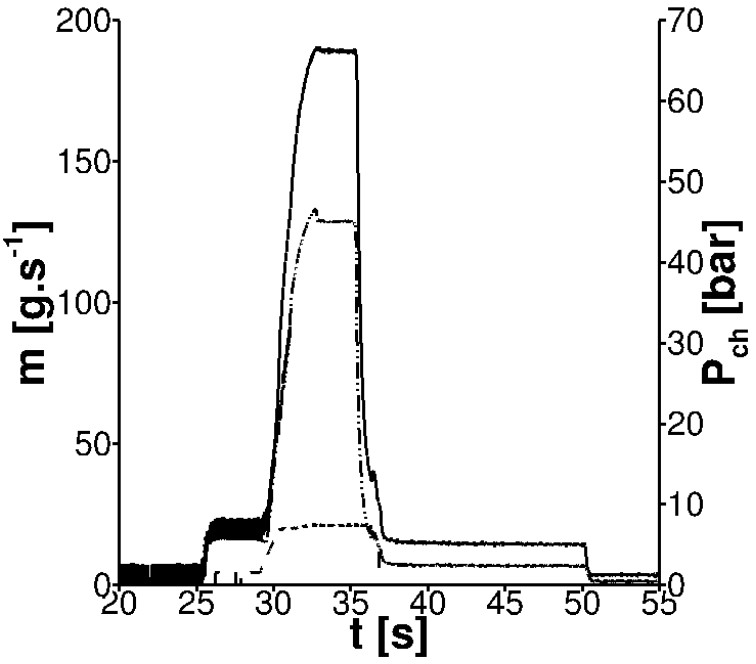

Fig. 4 Typical evolution of mass flow rates (O_2: -·-·- ; H_2: - - - -) and chamber pressure (——) during a hot-fire test.

walls are estimated with convective coefficients based on Colburn correlations [24], close to Bartz correlations [25, 26]. Following this design procedure, Fig. 5 presents the targeted operating points.

The objective of the present work is to study the influence of two parameters on heat transfer: the chamber pressure, P_{ch} and the mean oxidiser to fuel ratio, r. The operating range is here limited to reactants at ambient temperature so that two-phase and transcritical injection are not addressed in this study. The mean fuel to oxidiser momentum flux ratio, J, classically used to adress atomization process and flame evolution, is consequently directly linked to r as $J \simeq \frac{1}{r^2}$. Three values of P_{ch} (respectively, r) are targeted: 2, 4 and 6 MPa (respectively, 2, 4 and 7). The experimental

Case name	P_{ch} [MPa]	r [-]	J [-]
P2r4	1.90	3.9	0.8
P2r6	2.31	5.9	0.3
P4r2	4.13	1.8	3.6
P5r6	4.86	6.3	0.3
P5r7	5.11	6.9	0.2
P6r2	6.04	1.9	3.2
P6r3	6.16	3.2	1.1
P6r7	6.60	7.1	0.2
P6r7_L	6.31	7.7	0.2

Table 1 List of achieved operating points.

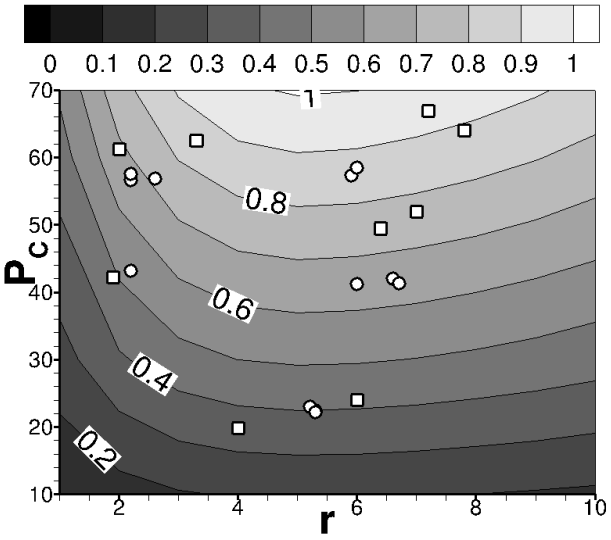

Fig. 5 Predicted map of normalised heat flux. The symbols denote all fire tests that have been performed: □ heat transfer setup; ○ visualisation setup.

conditions that were actually achieved during the various tests are reported in Tab. 1, together with the value of the momentum flux ratio at injection, J. The typical run-time for a hot fire is 12 s, with a steady combustion phase of a couple of seconds (cf. Fig. 4), except for case P6r7_L, which was run for more than 120 s. The objective of this longer run is the validation of the steady-state hypothesis for the evaluation of the heat fluxes.

B. Calibration procedure

All thermocouples were calibrated, prior to being fit into the combustion chamber. However, the principle of the brazing procedure is that a small amount of melted metal is used to 'glue' the thermocouple. Partial melting of the thermocouple tip may alter the calibration. Moreover, the accuracy of the final location of the brazed thermocouple is not known precisely. In order to make an a posteriori evaluation of these errors, an in-situ calibration procedure has been devised. It consists in inserting a temperature-controlled electrical heating device inside the chamber, which imposes a fixed homogeneous temperature on the hot side of the combustion chamber. The temperature is limited to about 400 K but it showed that all thermocouples have the same response except for four of them that were broken (three not responding and one with less than 40 % of the target temperature). These thermocouples are removed from the analysis. The uncertainties of the position of the thermocouples into their drilled holes can be as large as 1 mm (over a 8.5 mm distance between the thermocouples) so that a first estimate of the heat flux uncertainties is about 12% due to the uncertainties in the position of the thermocouples.

IV. Results

A. Temperature profiles on the two cylindrical segments

The temperature measurements from locations A, B and C (*cf.* Fig. 1(b)) are normalized by a reference temperature, T_r, which is the same for all operating conditions. The normalized temperature, defined as $\theta = T/T_r$, is then plotted versus the normalized longitudinal coordinate, $x^* = x/L_c$. Two typical results at a high mixture ratio ($r \sim 6$) are

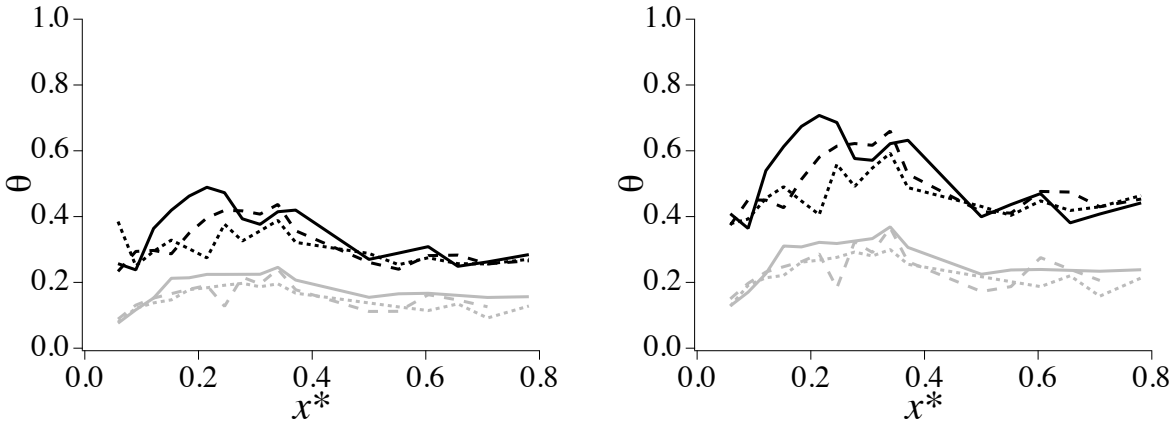

(a) P2r6. (b) P5r6.

Fig. 6 Reduced temperature profiles on the hot side (black) and cold side (grey), versus longitudinal coordinate for cases at mixture ratio $r = 6$. Location A (—— and ——); location B (····· and ·····); location C (- - - - and - - - -) in Fig. 1(b).

presented in Fig. 6, where grey lines refer to the cold side (thermocouples brazed in the material on the cooling channel side) and the black lines to the hot side (thermocouples brazed in the material on the combustion chamber side) of the combustion chamber. On both sides, the temperature reaches its maximum for $0.15 < x^* < 0.3$ and the temperature levels from location A are significantly higher than the other locations, which is consistent with the proximity of the outer injector (*cf.* Fig. 1(b)). Regarding locations B and C, no clear trend can be sorted out. Overall, the scattering of the data is quite low on the cold side, typically lower than 5%. On the hot side, the temperature signal is noisier, especially at location B, with oscillations between neighboring probes as large as 15% of the reference temperature.

Figures 6(a) and 6(b) both correspond to a mixture ratio $r \sim 6$ but different chamber pressures: $P_c \sim 2$ MPa and $P_c \sim 5$ MPa, respectively (*cf.* Tab. 1). The overall temperature profiles are very similar for both operating conditions, however, because the total power of case P5r6 is larger than that of case P2r6, the wall temperatures are higher on both sides. A similar trend is observed between cases P5r7 and P6r7, which are plotted in Fig. 7. Again, higher values of θ are reached because of the larger power resulting from the increase in pressure. Interestingly, for the high values of mixture ratio presented in Figs. 6 and 7, the longitudinal temperature profile on the hot side at location A consistently exhibits a 'double bump' shape with local maxima around $x^* = 0.2$ and $x^* = 0.35$. This particular shape is hardly

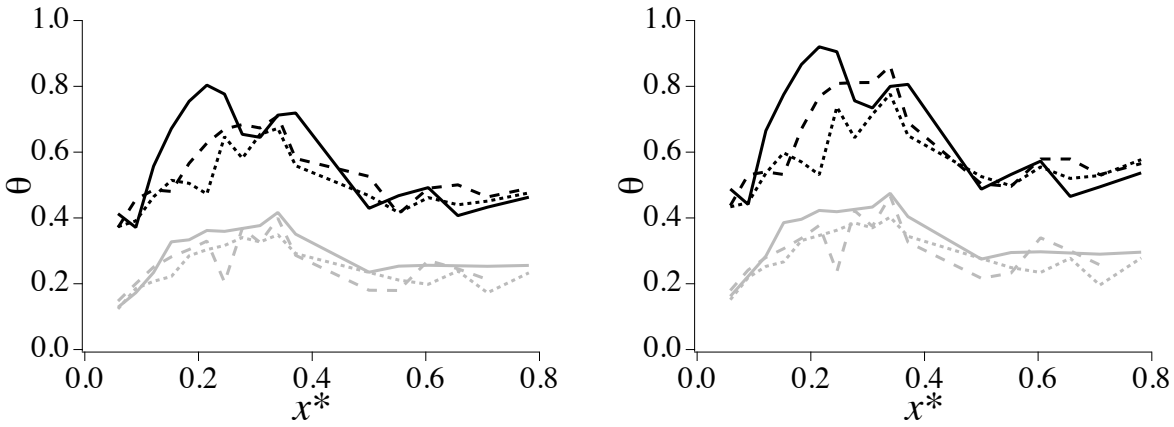

(a) P5r7. (b) P6r7.

Fig. 7 Reduced temperature profiles versus longitudinal coordinate for cases at mixture ratio $r = 7$. Same legend as Fig. 6.

visible at any of the other locations.

Another parameter that can have a great impact on the flame is the fuel to oxidiser momentum flux ratio, J. However, in these cases, which are gaseous only, this momentum ratio is directly linked to the mixture ratio r. The influence of this parameter is now investigated by decreasing it to $r = 4$ for the low pressure case ($P_c = 2$ MPa). The comparison

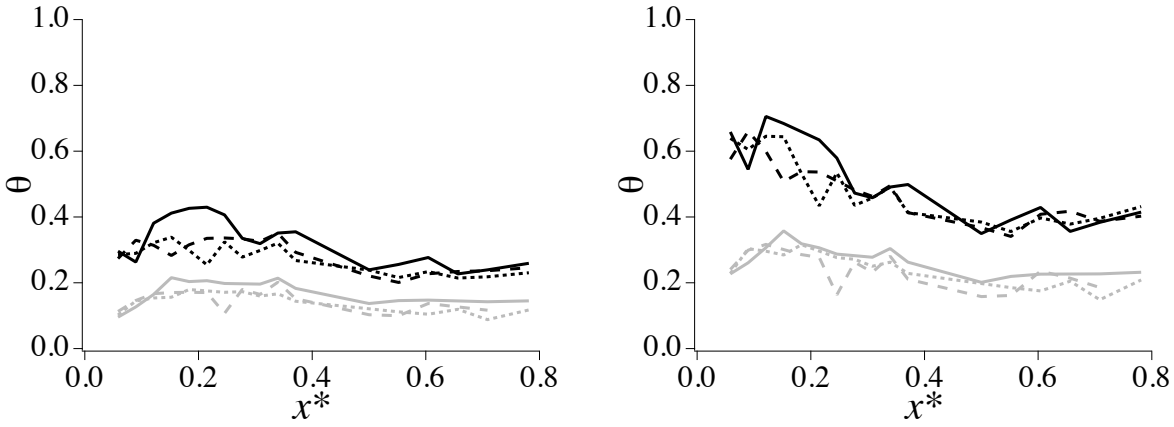

(a) P2r4. (b) P6r3.

Fig. 8 Reduced temperature profiles at intermediate mixture ratio. Same legend as Fig. 6.

of Figs. 6(a) and 8(a) shows that the general shape of the temperature profiles is not greatly affected between $r = 6$ and $r = 4$. The magnitude of the temperature variations is reduced on both sides but the double-bump shape is preserved. However, a further decrease to $r = 3$ yields a qualitative change (*cf.* Fig. 8(b)), especially on the hot side where the bumps are smoothed out and the reduced temperature is now very large at the entrance of the combustion chamber and exhibits a steep decrease until $x^* = 0.45$. This change is likely to have been caused by a modification of the flow field

and/or the flame shape in the combustion chamber. This hypothesis is discussed in Sec. C.

The results obtained with a further decrease of the mixture ratio to $r = 2$ are shown in Fig. 9. The change

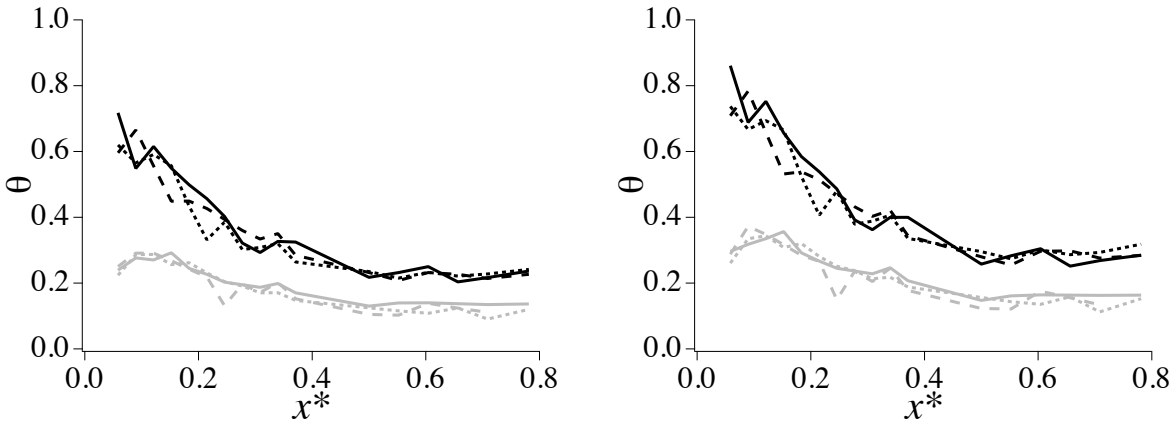

(a) P4r2. (b) P6r2.

Fig. 9 Reduced temperature profiles at low mixture ratio: $r = 2$. Same legend as Fig. 6.

is now drastic when compared to the high-mixture-ratio cases of Fig. 7: (1) the temperature profiles at the three azimutal locations are now virtually superimposed on both sides of the chamber wall and (2) the axial evolution is now monotonous on the hot side, with a steep decrease from $x^* = 0.1$ to $x^* = 0.45$ followed by a flat region. In fact, low mixture ratio cases corresponds here to high momentum flux ratio, leading to a quick flame opening and a strong recirculation zone at the beginning of the combustion chamber. Since the combustion process produces a diffusion flame, this flame burns at stoichiometric temperature. This very high temperature, along with a strong flame impingement early in the combustion chamber lead to very high temperature locally at the beginning of the combustion chamber.

It should be noted that for all cases, the temperature measurement at location C on the cold side (- - - -) exhibits a consistent dip around $x^* = 0.25$. It was originally thought that the thermocouple could be damaged but the calibration procedure described in Sec. B showed that this was not the case (at least in the limited temperature range that could be tested). We could not find another explanation for this dip so we are left to conjecture that it could be caused by a local inhomogeneity in the cooling.

The influence of the duration of the hot-fire run is assessed by performing case P6r7 over 120 s. This long run is denoted P6r7_L. The resulting reduced temperature profiles are presented in Figs. 7(b) and 10, respectively. The measurements at locations B and C are marginally affected when doubling the duration of the run at nominal condition. However, at location A, there is roughly a 10% increase of the temperature in the peak region. A possible explanation for this increase is that because of experimental uncertainties in the prescription of the flow rates, case P6r7_L is actually at a higher mixture ratio ($r = 7.7$ versus $r = 7$ for P6r7, cf. Tab. 1).Because the increase is consistent on the

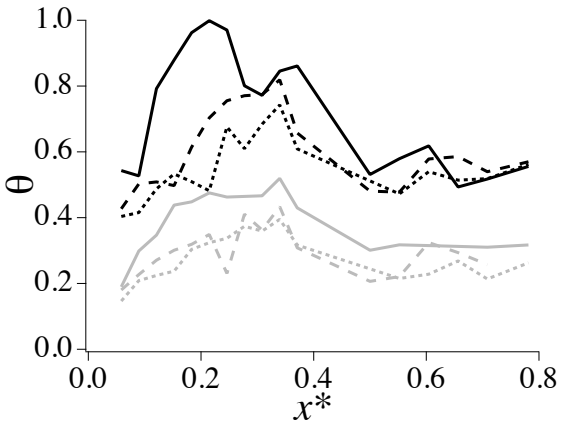

Fig. 10 Case P6r7_L: influence of run duration. Same legend as Fig. 6.

cold and hot sides, the corresponding heat flux is similar for both runs.

B. Heat fluxes

From previous temperature measurements, a methodology to extract heat fluxes can be designed. A 3D computation of heat transfer in steady state was conducted on a cylindrical solid body by imposing, on both sides, the temperature measurements obtained in experiments (in a dimensionning case, P6r7, see table 1), using bilinear interpolation in (r,θ) between measurement points. The symetry of the problem imposes to report the measurements on a 45° sector, which can induce artificial azimutal fluxes. The heat fluxes were then computed with both a full steady 3D approach and with simplified 1D radial approximation. The relative difference between 1D and 3D evaluations of heat transfer, presented in Fig.11, is lower than 12%, except for a single position, due to a suspicious large variation in the longitudinal and azimutal hot side temperature profile around this position (Fig.10). At almost all locations, this relative difference is less than 10% (light grey limit) between the two means of heat fluxes evaluations and at two thirds of them, the difference is less than 5% (dark grey limit), that seems sufficiently small to use 1D evaluation of heat transfer for all operating points.

It is now interesting to use the temperature profiles presented in Sec. A for the evaluation of the longitudinal evolution of the heat flux through the chamber walls. The procedure is the following: first, the temperature measurements at the three azimuthal locations (A, B and C, cf. Fig. 1(b)) are averaged, giving one mean value of the temperature on each side of the combustion-chamber wall. Then, the flux is evaluated by the resolution of the one-dimensional heat equation in cylindrical coordinates. This procedure assumes that radial fluxes are large compared to the azimuthal and longitudinal components.

The influence of pressure is discussed first. Figure 12(a) presents the longitudinal profiles of normalised radial heat

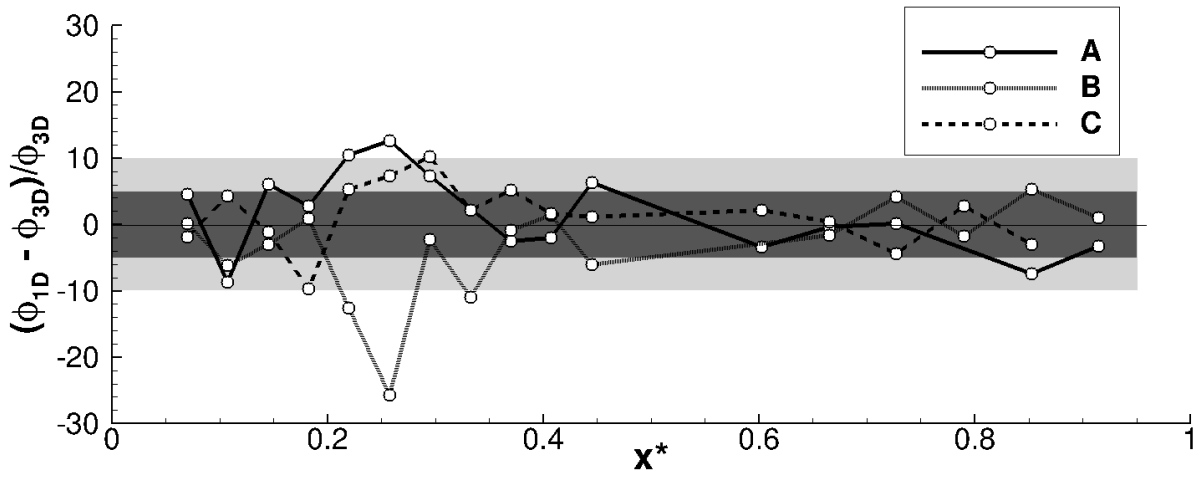

Fig. 11 Relative error between 1D and 3D computations of heat fluxes for case P6r7.

flux for the high mixture-ratio cases ($r \geq 6$). As anticipated from the temperature profiles, the fluxes increase with the

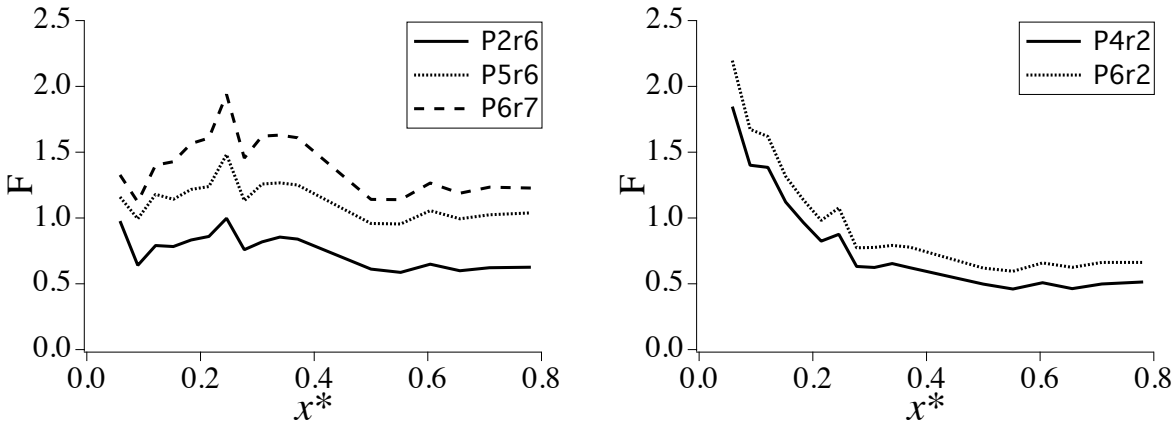

(a) High mixture ratio.

(b) Low mixture ratio.

Fig. 12 Longitudinal evolution of the normalised heat flux through the chamber wall. Influence of pressure for the low and high values of the mixture ratio.

chamber pressure, which results from the higher mass-flow rate and the subsequent increase in Reynolds number. The pressure ratio P5r6 over P2r6 is 2.1 and the one of P6r7 over P5r6 is 1.4. The heat fluxes presented in this figure shows that their evolution with the pressure is in agreement with the $P^{0.8}$ classical evolution.

The fluxes are consistently higher in the first half of the combustion chamber with a maximum around $x^* = 0.2$. After $x^* = 0.5$ the fluxes remain fairly constant. For these cases with a high mixture ratio, the variations of the heat fluxes are kept roughly within 20%. The situation is very different for the low mixture-ratio runs, which are presented in Fig. 12(b). Indeed, while the plateau is still visible for $x^* \geq 0.5$, there is a steep increase as one approaches the

injection plane. The peak heat flux at $x^* = 0.1$ is more than three times the downstream value. This behaviour is again speculated to originate from the flame length, deduced from OH* visualization, as it will be discussed in Sec.C. This heat flux evolution along the combustion chamber wall is very difficult to anticipate at the design stage with only correlation tools and without the help of higher order modelization such as CFD.

Indeed, the profiles of Fig. 12 are normalised in the same way as in Fig. 5, which was obtained a priori from correlations. There is less than 50% agreement between the predicted and measured values in the second half of the combustion chamber. In this region, there is no flame and the validity of the correlations for a flow of burnt gases in a tube is acceptable. The presence of the flame in the first half of the combustion chamber increases the fluxes by 50% to 200% of the value stemming from the correlation.

C. OH* visualization

Using the visualisation module described in Sec. B the influence of the mixture ratio on the flame shape is investigated. Two hot-fire runs at $P = 6$ MPa with a low and high mixture fraction are presented in Fig. 13. The exact operating conditions of Tab. 1 were not reproduced with the visualisation modules, nevertheless, they are close enough to discuss the qualitative influence of r on the flame shape. The field of OH* clearly reveals that the flame at $r = 2$ is much shorter than the one at $r = 5$. Moreover an intensity maximum is obtained at $x^* = 0.12$, corresponding to the position of the peak observed on Fig.12(b). This confirms the analysis of Fig.12, i.e. that the modified distribution of the fluxes correspond to the location of strongest OH* emission.

V. Conclusion and perspectives

In this study, a reduced-scale 5-injector rocket engine was used for the evaluation of heat fluxes in the combustion chamber. A collection of thermocouples brazed in the combustion-chamber walls was used to measure the material temperature on the flame and coolant sides. The heat fluxes were then reconstructed with the assumption that the radial component is predominant. The main conclusions of this study are that:

1) The mean fluxes increase with the pressure, which is to be expected because of the concomitant increase in Reynolds number in the chamber, and the classical evolution with $P^{0.8}$ is verified.
2) The mixture ratio has a strong impact on the longitudinal distribution of the heat fluxes as well as their peak value. For the high mixture-ratio cases, the longitudinal flux profiles only exhibit a smooth bump in the first half of the chamber. However, for the low values of the mixture ratio, the fluxes exhibit a steep increase as one approaches the injection faceplate.
3) The mixture ratio has also a strong impact on the azimuthal distribution of temperatures : with low mixture ratio (high momentum ratio), the temperature distribution is almost axisymmetrical, whereas it exhibits a strong variation with the azimuthal position with high mixture ratio and longer flames, which is probably due to greater

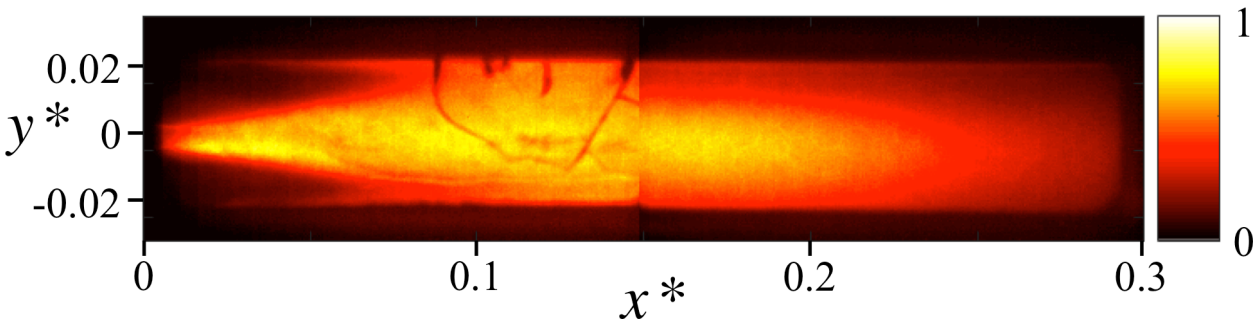

(a) Mixture ratio: $r = 2$.

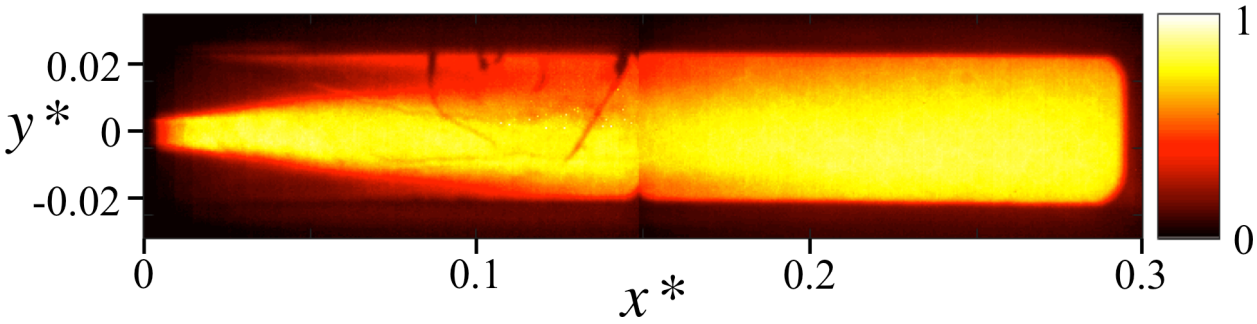

(b) Mixture ratio: $r = 5$.

Fig. 13 Influence of mixture ratio on the flame shape: time-averaged emission of OH* emission for a high-pressure run ($P = 6$ MPa).

interaction between the central and lateral flames.

Moreover, taking the downstream value of the heat flux (x^* between 0.6 and 0.8) as a reference, the peak value of the heat flux is around 20% higher for the high mixture ratio cases whereas at the lower mixture ratio, the peak can be as much as three times the reference. This indicates that, when designing the thermal resistance of the combustion chamber, classical correlations give a correct agreement with the mean downstream heat fluxes, but is not sufficient to predict the heat flux peak, which strongly depends on the flame topology. Although the integrated heat flux is, as expected, greater for high mixture ratio, the critical heat flux value to be retained for design is here obtained for low mixture ratio.

The setup was also equipped with optical access and the visualisation of spontaneous OH* emission allowed the determination of the mean flame shape. This measurement allowed to draw a parallel between the fluxes distribution and the flame shape. A shorter flame at the lower mixture ratio seemed to be the cause for the increased heat fluxes in the first half of the combustion chamber.

Compared to heat-sink combustion devices, this experiment is able to provide a steady state thermal environnement at the wall that gives access not only to heat fluxes but also to wall temperature, for different axial and azimuthal position in the chamber. Both are key parameters for rocket engine design. Heat fluxes are necessary to set up

operating conditions for a given performance, whereas wall temperature have to stay sufficiently low to ensure a given lifetime. However, those wall temperatures cannot be deduced precisely from wall heat fluxes, because uncertainties on heat fluxes imply much higher uncertainties on wall temperatures in such cooled devices. Indeed, the difference between hot gas temperature and wall temperature is generally large compared to absolute wall temperature. That is why this configuration brings a better level of characterisation compared to classical calorimeter devices, allowing CFD validation and heat transfer modeling on complementary data along the whole combustion chamber. At last, the possibility to gain optical access by replacing a thermal module by a visualization module that allows various optical diagnostics makes this experimental device quite unique in the liquid rocket engine community and a very valuable tool for CFD code validation. Indeed it would be a critical test for both the turbulent-combustion models, which would have to predict the flame shape, and for the wall models that would have to consistently evaluate the heat fluxes. Because multi-physics numerical simulation is also a growing trend in the combustion community, the configuration is also a benchmark for a three-code coupled simulation, resolving simultaneously the flow and combustion in the chamber, the heat transfer in the material and the water flow in the cooling channel. The development of such a methodology would be very useful as a design tool in the space propulsion industry.

All experiments presented in this paper were conducted in gaseous oxygen - gaseous hydrogen as it was the first campaign with that device. However, representative conditions with cold oxygen (liquid or supercritical) will be evaluated in further tests and will allow us to build a more complete validation database. Among other center of interests, one can cite the effect of the distance of the injectors to the chamber walls, the use of methane as fuel or the level of cooling. These effects will be investigated in future experimental campaigns.

Acknowledgements

This work has been conducted under a cooperation between CNES and ONERA. Most of data presented are proprietary. However, if interested, the reader is welcome to contact the corresponding author to discuss information exchange.

References

[1] Mayer, W. O. H., Schik, A. H. A., Vielle, B., Chauveau, C., G-ograve, I., kalp, Talley, D. G., and Woodward, R. D., "Atomization and Breakup of Cryogenic Propellants Under High-Pressure Subcritical and Supercritical Conditions," *Journal of Propulsion and Power*, Vol. 14, No. 5, 1998, pp. 835–842
doi:10.2514/2.5348.

[2] Fröhlich, A., Popp, M., Schmidt, G., and Thelemann, D., "Heat Transfer Characteristics of H2/O2 Combustion Chambers," AIAA paper 1993-1826, 1993
doi:10.2514/6.1993-1826.

[3] Marshall, W., Pal, S., Woodward, R., and Santoro, R., "Benchmark Wall Heat Flux Data for a GO2/GH2 Single Element Combustor," AIAA paper 2005-3572, 2005, pp. 1–13
doi:10.2514/6.2005-3572.

[4] DeRidder, M. A., and Anderson, W. E., "Heat Flux and Pressure Profiles in an Oxygen/Hydrogen Multielement Rocket Combustor," *Journal of Propulsion and Power*, Vol. 26, No. 4, 2010, pp. 696–705
doi:10.2514/1.48060.

[5] Conley, A., Vaidyanathan, A., and Segal, C., "Heat Flux Measurements for a GO2/GH2 Single-Element, Shear Injector," *Journal of Spacecraft and Rockets*, Vol. 44, No. 3, 2007, pp. 633–639
doi:10.2514/1.26678.

[6] Cai, G., Li, M., Gao, Y., and Jin, P., "Simulation and Experiment Research for a Hydrogen-Rich/Oxygen-Rich Shear Tricoaxial Gas-Gas Injector," AIAA paper 2010-6740, Reston, Virigina, 2010
doi:10.2514/6.2010-6740.

[7] Silvestri, S., Maria Palma, C., Kirchberger, C., Schlieben, G., Haidn, O., and Knab, O., "Investigation on Recess Variation of a Shear Coax Injector for a Single Element GOX-GCH4 Combustion Chamber," Vol. 14, 2016, pp. 13–20.

[8] Celano, M. P., Silvestri, S., Bauer, C., Perakis, N., Schlieben, G., and Haidn, O. J., "Comparison of Single and Multi-Injector GOX/CH4 Combustion Chambers," AIAA paper 2016-4990, 2016
doi:10.2514/6.2016-4990.

[9] Daimon, Y., Negishi, H., Koshi, M., and Suslov, D., "Numerical and Experimental Investigation of the Methane Film Cooling in Subscale Combustion Chamber," *Progress in Propulsion Physics*, Vol. 8, 2016, pp. 129–144
doi:10.1051/eucass/201608129.

[10] Arnold, R., Suslov, D. I., and Haidn, O. J., "Experimental Investigation of Film Cooling with Tangential Slot Injection in a LOX/CH4 Subscale Rocket Combustion Chamber," *Transactions of the Japan Society for Aeronautical and Space Sciences, Space Technology Japan*, Vol. 7, 2009, pp. 81–86
doi:10.2322/tstj.7.pa_81.

[11] Arnold, R., Suslov, D., and Haidn, O. J., "Film Cooling of Accelerated Flow in a Subscale Combustion Chamber," *Journal of Propulsion and Power*, Vol. 25, No. 2, 2009, pp. 443–451
doi:10.2514/1.39308.

[12] Arnold, R., Suslov, D., and Haidn, O., "Circumferential Film Cooling Effectiveness in a LOX/H2 Subscale Combustion Chamber," *Journal of Propulsion and Power*, Vol. 25, No. 3, 2009, pp. 760–770
doi:10.2514/1.40305.

[13] Arnold, R., Suslov, D. I., and Haidn, O. J., "Film Cooling in a High-Pressure Subscale Combustion Chamber," *Journal of Propulsion and Power*, Vol. 26, No. 3, 2010, pp. 428–438

doi:10.2514/1.47148.

[14] Ahn, K., Kim, J.-G., and Choi, H.-S., "Effects of Injector Recess on Heat Flux in a Combustion Chamber With Cooling Channels," *Aerospace Science and Technology*, Vol. 37, 2014, pp. 110–116
doi:10.1016/j.ast.2014.05.012.

[15] Ordonneau, G., Hervat, P., Vingert, L., Petitot, S., and Pouffary, B., "First Results of Heat Transfer Measurements in a New Water-Cooled Combustor on the Mascotte Facility," *4th European Conference for Aeronautics and Space Sciences*, St Petersburg, 2011.

[16] Fdida, N., Vingert, L., Ordonneau, G., and Petitot, S., "Coupling High-Speed Imaging Diagnostics to Study a LOX/GH2 Flame in a High-Pressure Rocket Combustor," *5th European Conference for Aeronautics and Space Sciences*, Munich, 2013, pp. 1–13.

[17] Vingert, L., Ordonneau, G., Fdida, N., and Grenard, P., "A Rocket Engine Under a Magnifying Glass," *AerospaceLab*, , No. 11, 2016, p. 15.

[18] Habiballah, M., Orain, M., Grisch, F., Vingert, L., and Gicquel, P., "Experimental Studies of High-Pressure Cryogenic Flames on the Mascotte Facility," *Combustion Science and Technology*, Vol. 178, No. 1-3, 2006, pp. 101–128
doi:10.1080/00102200500294486.

[19] Pietzka, G., "The Spectroscopy of Flames, von A. G. Gaydon. Chapman & Hall Ltd., London 1957. 1. Aufl., IX, 279 S., geb. £ 2.10.0," *Angewandte Chemie*, Vol. 70, No. 19, 1958, pp. 613–613
doi:10.1002/ange.19580701915.

[20] Sardeshmukh, S., Bedard, M., and Anderson, W., "The Use of OH* and CH* as Heat Release Markers in Combustion Dynamics," *International Journal of Spray and Combustion Dynamics*, Vol. 9, No. 4, 2017, pp. 409–423
doi:10.1177/1756827717718483.

[21] Fiala, T., Sattelmayer, T., Gröning, S., Hardi, J., Stützer, R., Webster, S., and Oschwald, M., "Comparison Between Excited Hydroxyl Radical and Blue Radiation from Hydrogen Rocket Combustion," *Journal of Propulsion and Power*, Vol. 33, No. 2, 2017, pp. 490–500
doi:10.2514/1.b36280.

[22] Candel, S., Juniper, M., Singla, G., Scouflaire, P., and Rolon, C., "Structure and Dynamics of Cryogenic Flames at Supercritical Pressure," *Combustion Science and Technology*, Vol. 178, No. 1-3, 2006, pp. 161–192
doi:10.1080/00102200500292530, URL https://doi.org/10.1080/00102200500292530.

[23] Dieke, G., and Crosswhite, H., "The ultraviolet bands of OH Fundamental data," *Journal of Quantitative Spectroscopy and Radiative Transfer*, Vol. 2, No. 2, 1962, pp. 97–199
doi:10.1016/0022-4073(62)90061-4.

[24] Colburn, A., "A Method of Correlating Forced Convection Heat Transfer Data and a Comparison With Fluid Friction," *Trans. AIChE Journal*, Vol. 29, 1933, pp. 174–210.

[25] Bartz, D. R., "A Simple Equation for Rapid Estimation of Rocket Nozzle Convective Heat Transfer Coefficients," *Jet Propulsion*, 1957, pp. 49–51.

[26] Bartz, D. R., "Turbulent Boundary-Layer Heat Transfer From Rapidly Accelerating Flow of Rocket Combustion Gases and of Heated Air," *Advances in Heat Transfer*, Vol. 2.